Supplementary Note 6: Numerical Validation

a) Numerical Tests for Surface Diffusion

A series of numerical test is conducted to assess the performance of the surface diffusion on a cubic grid. We use the test suggested in [1].

Diffusion on a sphere

The following asymmetric solution

$$C(\theta, \psi, t) = 2 + \frac{1}{2} e^{-2t} \cos\psi \sin\theta + e^{-6t} \cos 2\psi \sin^2\theta + e^{-12t} \cos 3\psi \sin^3\theta \quad (1)$$

of the diffusion equation

$$\frac{\partial C}{\partial t} = \frac{1}{\sin\theta} \frac{\partial}{\partial \theta} \left(\sin\theta \frac{\partial C}{\partial \theta} \right) + \frac{1}{\sin^2\theta} \frac{\partial^2 C}{\partial \theta^2}$$

on a unit sphere will will be used as a reference for comparisons with the numerical algorithm.

The initial condition of the numerical solution is constructed by populating each surface element with a concentration given by $C(\theta_c, \psi_c, t)$, where θ_c and ψ_c are the position of the center of a surface element in spherical coordinates.

We assess the performance of the method by running the simulation using resolutions ranging from 5 to 157 grid elements with side length h for the diamater of the sphere. Additionally the distance Δk between surface elements used to estimate the local curvature is varied between 2 and 39. Each simulation is integrated untill $t = 1$.

Supplementary Figure 9 shows the largest relative error that occured over the course of the individual simulations as a function of the diameter of the sphere meassured in grid elements. Symbols with common shapes and colors represent simulations with common distance Δk used for estimating the local curvature. The maximum error shows two distict behaviors for a given distance Δk, for small numbers of grid elements, i.e. large grid constants, reductions of the grid constants lead to a reduction of the error following a power law. However, this relation only holds up untill a certain Δk dependent grid size.

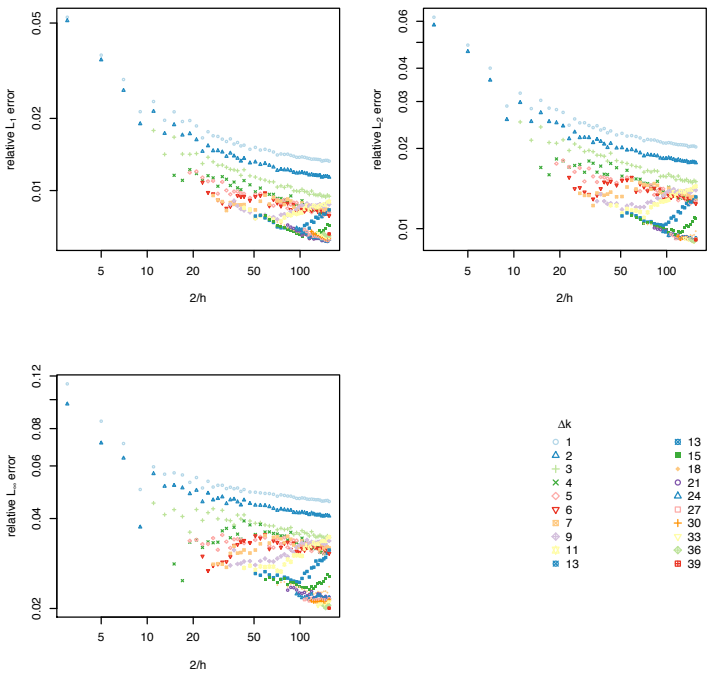

Supplementary Figure 9: Maximum relative error in L_1, L_2 and L_∞ norm as a function of the grid size used in the simulation. Symbol shapes and colors indicate the distance Δk used for curvature estimation.

For smaller grid constants the errors do either decrease with a smaller power or begin to oscillate. Thus in order to take advantage of larger grid sizes Δk has to be adapted. Comparing the different error norms shows no qualitative difference between these norms.

Supplementary Figure 10 shows the time dependence of the mean square error for simulations with different grid constants and step sizes. The initial contition is set up to match the analytic solution exactly, which leads to a sharp rise of the error at the beginning of the simulation. Local disretization errors in regions with high concentration gradients lead to an initial growth of the error. These error terms are dissipated over time by the diffusion, while discretization errors contribute less to the error of the solution due to shallower concentration gradients, which is reflected by the decreasing error as the simulations continue.

Supplementary Figure 11(a) illustrates the dependence of the maximum L_2 error of a simulation on the step size Δk for a mid-resolution simulation. For small Δk an increase of the step size leads to a decrease of the maximum L_2 error of a simulation, however for step sizes larger than a grid constant

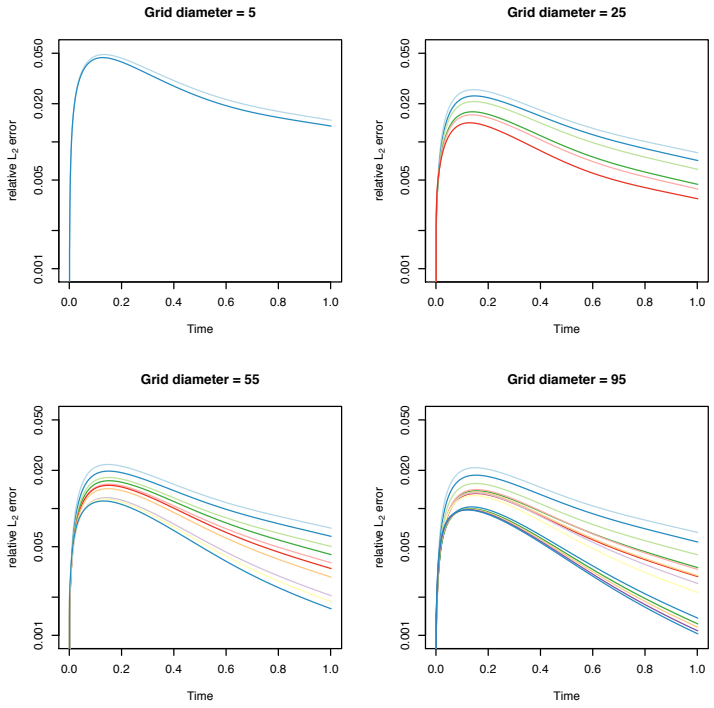

Supplementary Figure 10: Relative error in L_2 norm as a function of time. Line colors indicate the distance Δk used for curvature estimation.

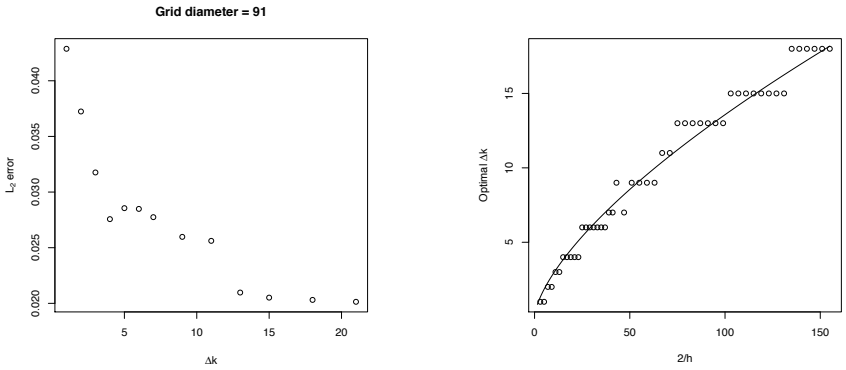

(a) Effect of increasing the distance Δk for a given grid diameter.

(b) Optimal choice of the distance Δk for varying grid diameters. Points indicate results from numerical experiments, the solid line shows the theoretical optimum $\Delta k = h^{-2/3}$

Supplementary Figure 11: Step size Δk affects the simulation performance.

dependent threshold the error will begin to oscillate with further increases of the step size Δk.

The optimal step size Δk for estimating the local surface curvature is given in [1] as $\Delta k = h^{-2/3}$. Since h can be interpreted as the inverse radius of the sphere in grid constants we can estimate the optimal value of Δk for arbitrary shapes by defining the scale at which a sphere of a given radius is optimaly sampled. sphere of a **Supplementary Figure 11(b)** shows the optimal Δk obtained in numerical experiments. Values of Δk at a given grid constant are assessed by comparing the largest relative L_2 error that occured in each simulation. A naive approach to choose the optimal value would be to pick the Δk for which the maximum error occuring during a simulation is smallest. However, **Supplementary Figure 11(a)** shows that the error is nearly independend from the step size after a certain threshold is exceeded. This weak complex dependency of the error on Δk and the grid constant can be considered noise for all practical purposes. Therefore, a value Δk is considered optimal if it is the smallest Δk that has an associated L_2 error that is within 10% of the smallest observed error.

Supplementary Figure 13 illustrates the effect of the local adaption procedure on the geometry of the sphere. As described in the main text and **Supplementary Note 3d**, the geometry of the surface of the cubic grid is adapted to approximate a curved surface. The visualizations in **Supplementary Figure 13** rely on surface normals, which are derived from the adapted geometry, as an input to the shading model that illuminates the visualization. The vertex normals that enter the shading model itself are the average of the surface normals

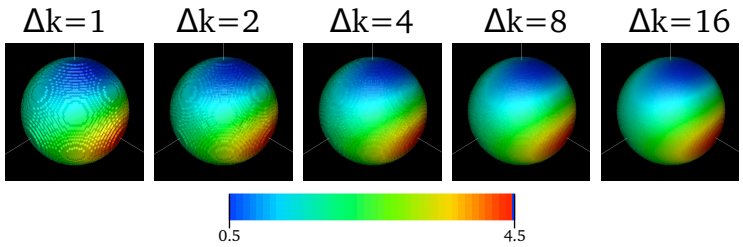

Supplementary Figure 13: Visualization of the effect of increasing step size Δk. The heatmap shows the concentration in arbitrary units.

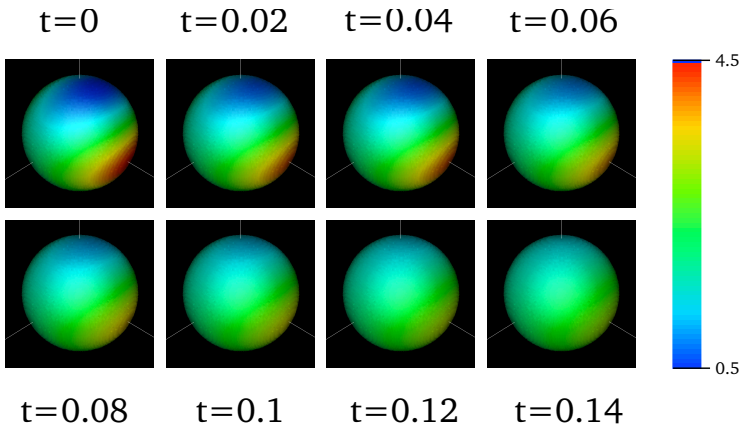

Supplementary Figure 14: Visualization of the simulation used to test the accuracy of the numerical solution of the diffusion equations. The heatmap shows the concentration in arbitrary units.

of the surfaces sharing the vertex under consideration.

Supplementary Figure 14 visualizes the numerical solution of the diffusion equation with the initial conditions given by the solution (Equation 1) for $t = 0$. The method of interpolating the surface normals described above is employed here as well.

Supplementary Figure 15 shows the magnitude of the local relative error for simulations with varying resolution. As most changes to the error occur during the first half of the simulation the error is only shown up till $t = 0.4$. The viewpoint corresponds to Figure 14, comparing the solution with the error, it becomes obvious that the largest errors occur in the regions with the steepest gradients. As the gradients become shallower the magnitude of the error decreases.

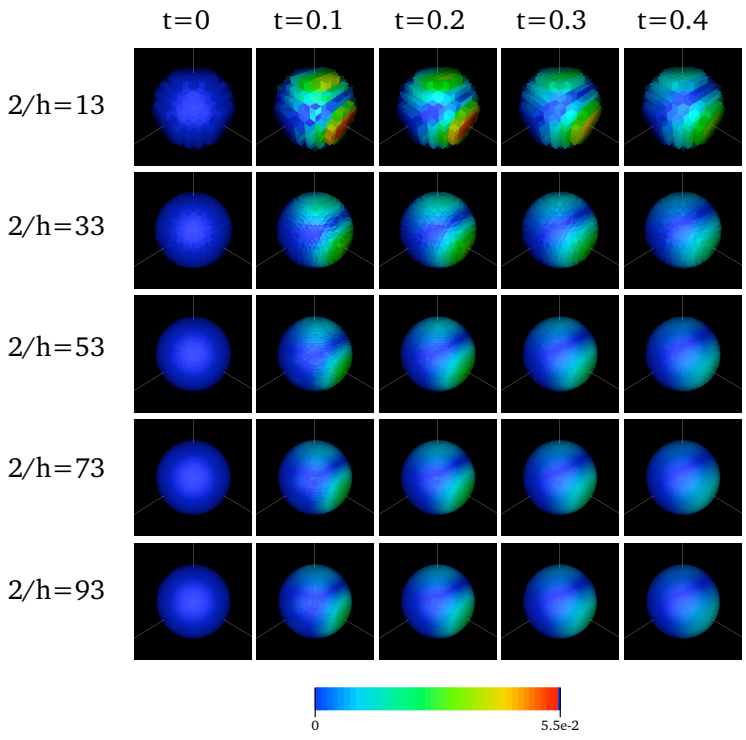

Supplementary Figure 15: Visualization of distribution of the relative error.

References

[1] I. L. Novak, F. Gao, Y.-S. Choi, D. Resasco, J. C. Schaff, B. M. Slepchenko, *Diffusion on a Curved Surface Coupled to Diffusion in the Volume: Application to Cell Biology.*, J Comput Phys. 2007 Oct 1;226(2):1271-1290.

b) Numerical Tests for 3-Dimensional (Bulk) Diffusion

We test the accuracy of the 3-dimensional (bulk) diffusion algorithms in Simmune by using the analytical solution of the diffusion equation on a box with no flux boundary conditions, a side length L and a diffusing particle with diffusion constant D.

$$c(t,x,y,z) = \sum_{i,j,k=0}^{\infty} a_{ijk} \cos\left(\frac{i\pi x}{L}\right) \cos\left(\frac{j\pi y}{L}\right) \cos\left(\frac{k\pi z}{L}\right) \cdot \exp\left(-Dt\left(\left(\frac{i\pi}{L}\right)^2 + \left(\frac{j\pi}{L}\right)^2 + \left(\frac{k\pi}{L}\right)^2\right)\right) \quad (1)$$

We set the side length of the box to $L = 15\,\mu m$, and choose a a rather conservative value for the diffusion constant of $D = 10^{-12}\frac{m^2}{s}$, describing the slow diffusion of a large scaffold protein complex. In order to produce biologically plausible concentration fields we assume that the coefficient $a_{ijk} = 0$ for all i, j or k larger than 3. The coefficient a_{000} determines the average concentration, which we set to $0.4\,\mu mol/l$. All other coefficients are set to

$$a_{ijk} = \rho \frac{10^{-8}}{i+j+k+1},$$

where $\rho \in \{0 \dots 5\}$ is an integer drawn from a uniform random distribution. The factor $(i+j+k+1)^{-1}$ is introduced to suppress highly oscillating components leading to unrealistically steep gradients in the initial distribution of the diffusing molecule.

In order to get a better understanding of the concentration distributions used in this analysis, we choose one representative distribution and plot an axis parallel slice for through the location of the steepest gradient, choosing the slice orthogonal to the smallest component of the gradient.

Discretization error due to undersampling

First we asses the discretization error due to undersampling the exact distribution. When setting the initial condition of the numerical solution we have the choice to set the numerical concentration of each voxel to the average of the exact concentration integrated over the voxel, or to set the numerical concentration of each voxel to the exact concentration sampled at a single point e.g. the center of the voxel.

We set the initial condition of the numerical solution employing the first method, thereby ensuring that the average concentration (i.e. total number of molecules) introduced into the numerical simulation matches the average concentration in the exact solution.

Supplementary Figure 17 shows the distribution of the errror for $n = 40$ different concentration distributions for a range of grid resolutions. The error of the numerical solution in meassures in the L_∞-norm thus capturing effects such as anisotropic diffusion due to discretization artifacts. We scale the L_∞-norm by the exact value of the concentration at the point at which the absolute differences between exact and numeric concentration is maximal. The discretization converges to the exact solution, as expected. This however, merly shows the correct setting of the initial conditions.

In **Supplementary Figure 18** we observe the relation between the maximal observed error and the maximal discretized gradient. Each Line in the figure connects the same concentration distribution observed at different resolutions. The lowest grid resolutions are unable to captute the actual gradients, which leads to the increase of the observed gradient for a given distribution.

Discretization error of the numerical solution

Supplementary Figure 18 shows the time course of the L_∞ error for $n = 40$ different initial conditions for grid resolutions ranging from 6 to 48 voxels. The qualitative behaviour of the error does not depend on the grid resolution. We observe conververgence of the error with decreasing voxel size. The fast decay of the error by an order of magnitude within the first two seconds of the simulation is due to the fast decay of high frequence modes in diffusive processes. The frequencies i, j, k enter the time dependent factor $T(t)$ of

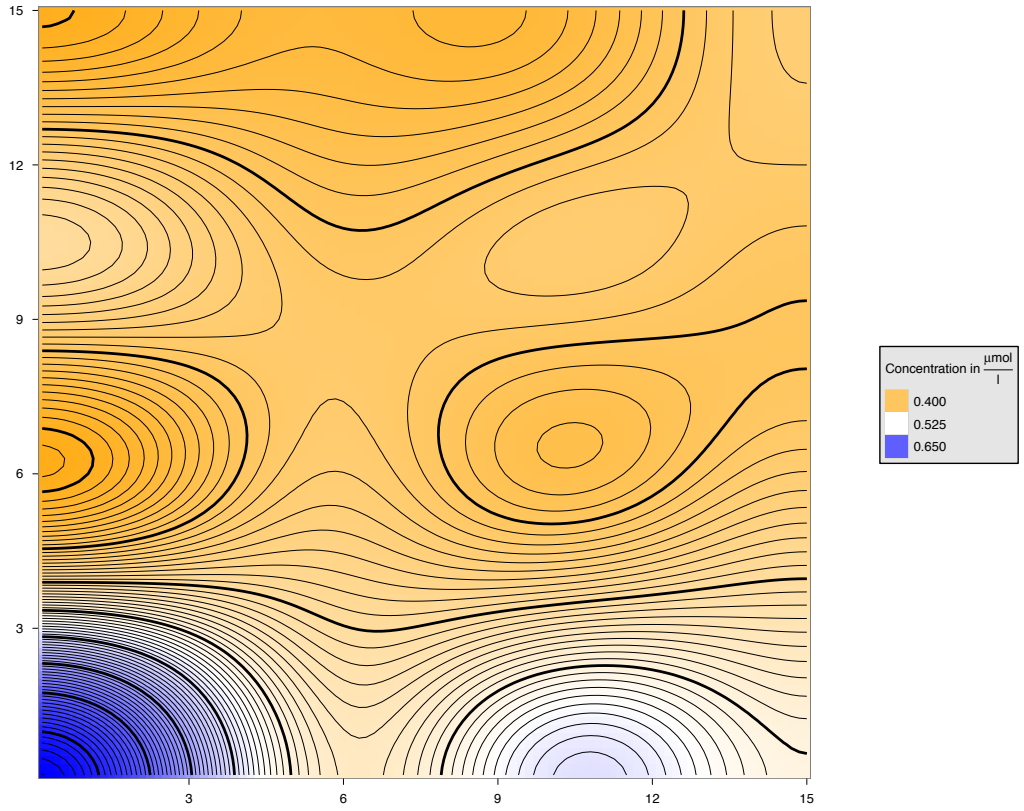

Supplementary Figure 16: Visualization of a concentration distribution in the plane containing the maximum in plane gradient. The concentrations are color coded as indicated in the figure legend, lines indicate locations of equal concentrations. Thick lines are plotted at intervalls of $50\,nmol/l$, thin lines at intervalls of $5\,nmol/l$.

the solution of the diffusion equation (2) quadratically

$$T(t) = \exp\left(-Dt\left(\left(\frac{i\pi}{L}\right)^2 + \left(\frac{j\pi}{L}\right)^2 + \left(\frac{k\pi}{L}\right)^2\right)\right). \tag{2}$$

The high frequency terms of the inital discretization error decay together with the high frequency terms of the solution.

The error increases over the next few seconds before decaying with the expected suppression $\propto \exp(-t)$. This is due to low frequency error modes that stem from the anisotropy of the discretized laplacian, and lead to slower diffusion near concentration extrema, as can be seen if **Supplementary Figure 20**. However, even for very low diffusion constants of $D = 10^{-12}\frac{m^2}{s}$ and coarse dircretizations with voxel sizes on the order of one micron the relative error decays to values below 10^{-3} within $10\,s$.

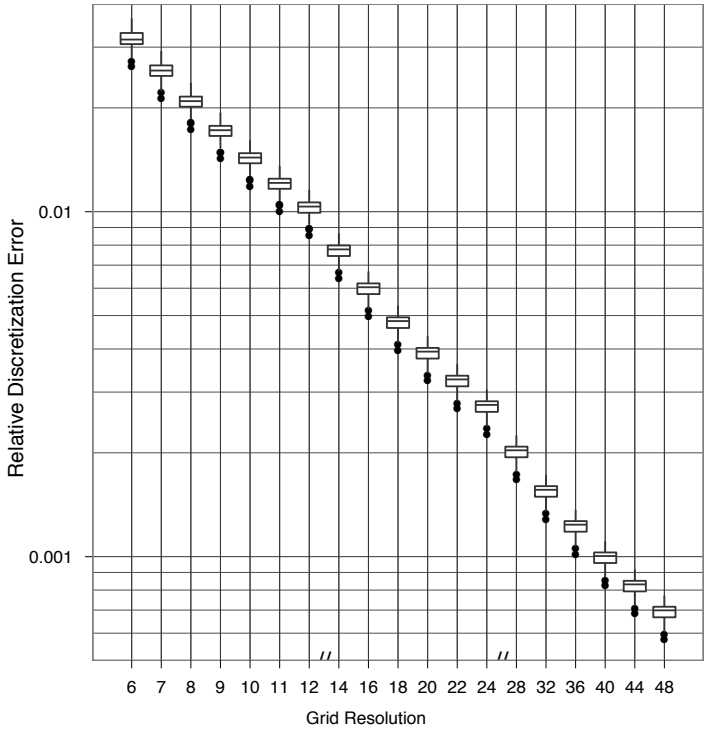

Supplementary Figure 17: Distribution of relative L_∞-errors at $t = 0$. Boxes show the 1^{st}, 2^{nd}, 3^{rd} quartile, whiskers extend 3/2 interquartile ranges ($n = 40$).

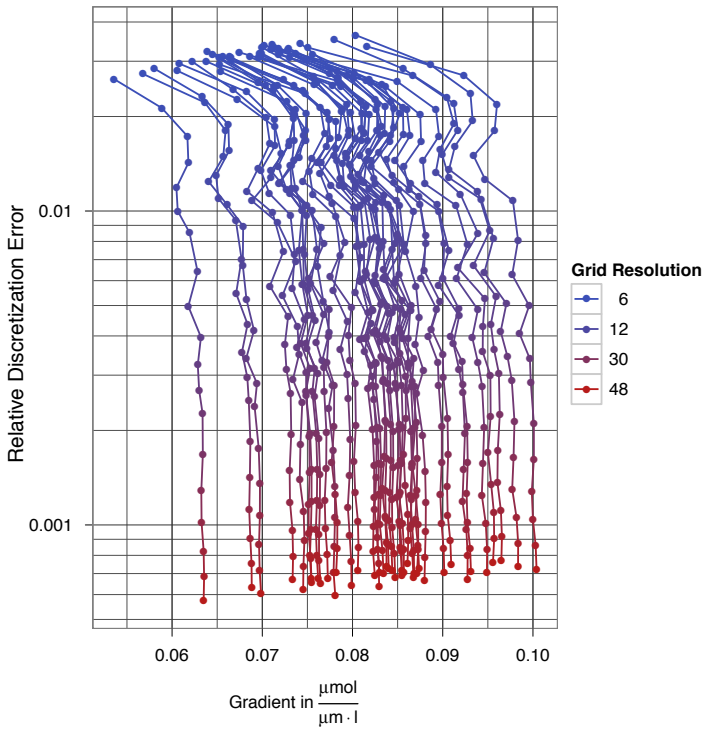

Supplementary Figure 18: Relationship between the discretization error and gradient strength. Values corresponding to the same set of coefficients a_{ijk} are connected by lines to improve readability.

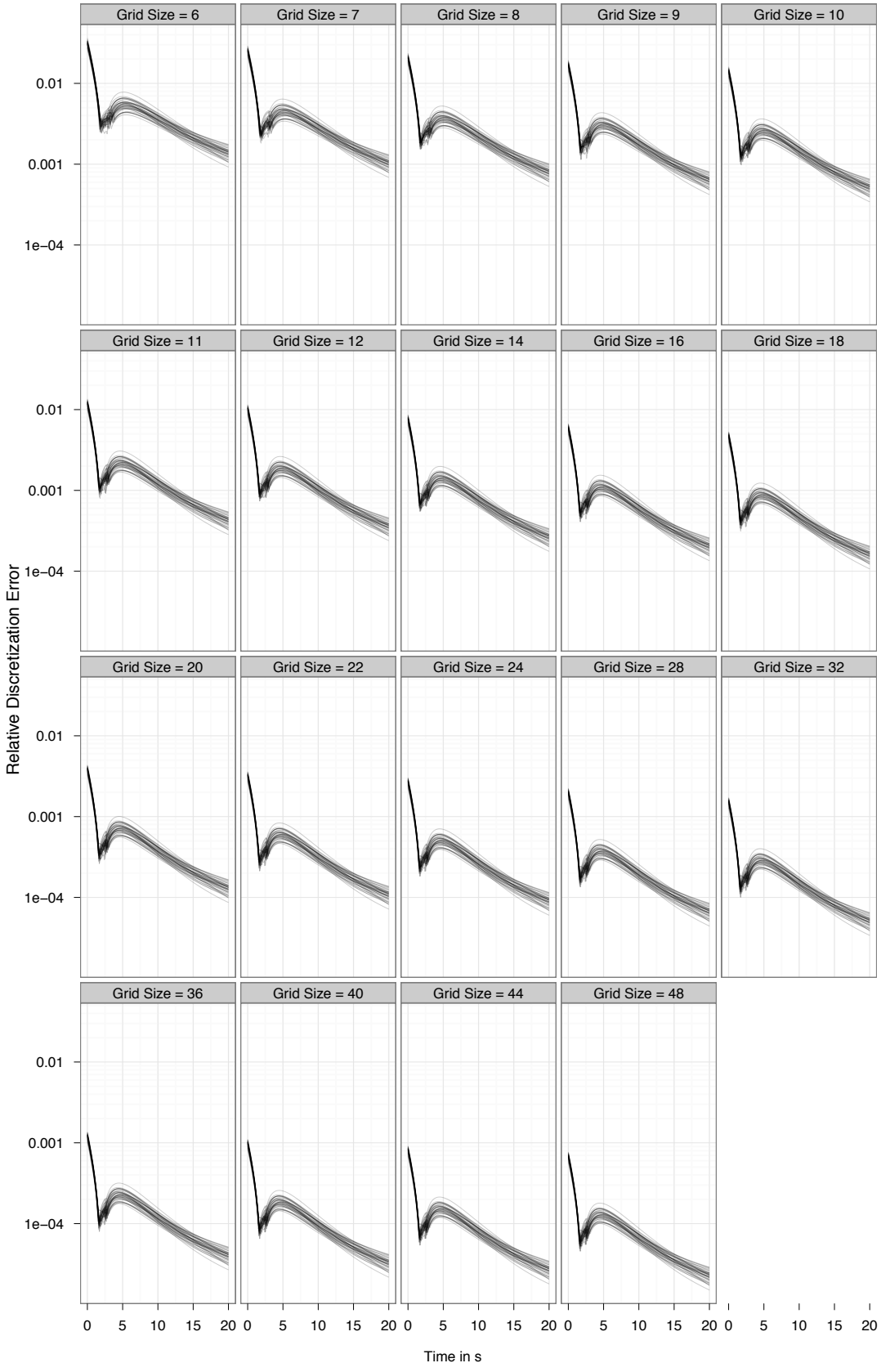

Supplementary Figure 19: Time course of the L_∞ error for $n = 40$ random initial concentration distributions for grid resolutions ranging from 6 to 48 voxels.

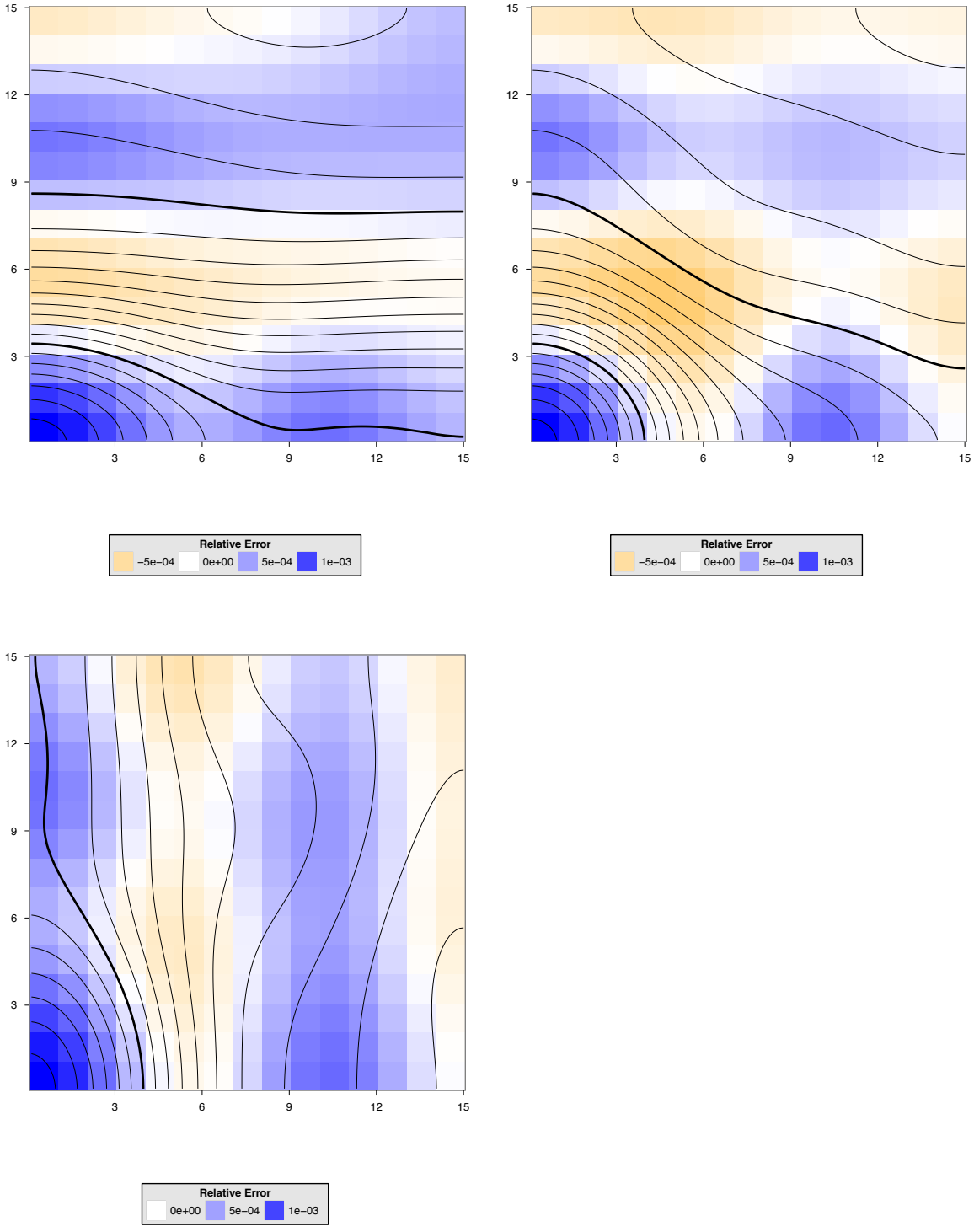

Supplementary Figure 20: Visualization of the relative L_∞ error at $t = 5\,s$ using voxels with a side length of $1\,\mu m$. The relative L_∞ error is color coded as indicated in the figure legend, lines indicate locations of equal concentrations. Thick lines are plotted at intervalls of $50\,nmol/l$, thin lines at intervalls of $5\,nmol/l$. The first panel corresponds to the slice orientation displayed in figure 16.